

Optical malignancy parameters for monitoring progression of breast cancer neoadjuvant chemotherapy

David R. Busch,^{1*} Regine Choe,² Mark A. Rosen,³ Wensheng Guo,⁴ Turgut Durduran,⁵ Michael D. Feldman,⁶ Carolyn Mies,⁶ Brian J. Czerniecki,⁷ Julia Tchou,⁷ Angela DeMichele,⁸ Mitchell D. Schnall,³ and Arjun G. Yodh,¹

¹Dept. of Physics and Astronomy, University of Pennsylvania, 209 S. 33rd St., Philadelphia, PA 19104 USA

²Dept. of Biomedical Engineering, University of Rochester NY 14627 USA

³Dept. of Radiology, University of Pennsylvania, PA 19104 USA

⁴Dept. of Biostatistics, University of Pennsylvania, PA 19104 USA

⁵Institut de Ciències Fotòniques, Castelldefels, Barcelona Spain

⁶Dept. of Pathology and Laboratory Medicine, University of Pennsylvania, PA 19104 USA

⁷Dept. of Surgery, University of Pennsylvania, PA 19104 USA

⁸Depts. of Medicine (Hematology/Oncology) and Epidemiology, University of Pennsylvania, PA 19104 USA

[*drbusch@sdf.org](mailto:drbusch@sdf.org)

Abstract: We introduce and demonstrate use of a novel, diffuse optical tomography (DOT) based breast cancer signature for monitoring progression of neoadjuvant chemotherapy. This signature, called probability of malignancy, is obtained by statistical image analysis of total hemoglobin concentration, blood oxygen saturation, and scattering coefficient distributions in the breast tomograms of a training-set population with biopsy-confirmed breast cancers. A pilot clinical investigation adapts this statistical image analysis approach for chemotherapy monitoring of three patients. Though preliminary, the study shows how to use the malignancy parameter for separating responders from partial-responders and demonstrates the potential utility of the methodology compared to traditional DOT quantification schemes.

© 2012 Optical Society of America

OCIS codes: (170.3830) Mammography; (170.3880) Medical and biological imaging; (170.1610) Clinical applications; (170.6510) Spectroscopy, tissue diagnostics.

References and links

1. M. Kaufmann, G. von Minckwitz, H. D. Bear, A. Buzdar, P. McGale, H. Bonnefoi, M. Colleoni, C. Denkert, W. Eiermann, R. Jackes, A. Makris, W. Miller, J.-Y. Pierga, V. Semiglazov, A. Schneeweiss, R. Souchon, V. Stearns, M. Untch, and S. Loibl, "Recommendations from an international expert panel on the use of neoadjuvant (primary) systemic treatment of operable breast cancer: new perspectives 2006," *Ann. Oncol.* **18**, 1927–34 (2007).
2. L. R. Arlinghaus, X. Li, M. Levy, D. Smith, E. B. Welch, J. C. Gore, and T. E. Yankelev, "Current and future trends in magnetic resonance imaging assessments of the response of breast tumors to neoadjuvant chemotherapy," *J. Oncol.* **919620**, 1–17 (2010).
3. L. Esserman, D. Berry, M. Cheang, C. Yau, C. Perou, L. Carey, A. DeMichele, J. Gray, K. Conway-Dorsey, M. Lenburg *et al.*, "Chemotherapy response and recurrence-free survival in neoadjuvant breast cancer depends on biomarker profiles: results from the I-SPY 1 TRIAL (CALGB 150007/150012; ACRIN 6657)," *Breast Cancer Res. Treat.* **30**, 3242–3249 (2011).

4. K. McGuire, J. Toro-Burguete, H. Dang, J. Young, A. Soran, M. Zuley, R. Bhargava, M. Bonaventura, R. Johnson, and G. Ahrendt, "MRI staging after neoadjuvant chemotherapy for breast cancer: Does tumor biology affect accuracy?" *Ann. Surg. Oncol.* **18**, 3149–3154 (2011).
5. O. Falou, H. Soliman, A. Sadeghi-Naini, S. Iradji, S. Lemon-Wong, J. Zubovits, J. Spayne, R. Dent, M. Trudeau, J. Boileau *et al.*, "Diffuse optical spectroscopy evaluation of treatment response in women with locally advanced breast cancer receiving neoadjuvant chemotherapy," *Trans. Onc.* **5**, 238–246 (2012).
6. D. Roblyer, S. Ueda, A. Cerussi, W. Tanamai, A. Durkin, R. Mehta, D. Hsiang, J. A. Butler, C. McLaren, W.-P. Chen, and B. Tromberg, "Optical imaging of breast cancer oxyhemoglobin flare correlates with neoadjuvant chemotherapy response one day after starting treatment." *Proc. Natl. Acad. Sci.* **108**, 14626–14631 (2011).
7. R. Choe and T. Durduran, "Diffuse optical monitoring of the neoadjuvant breast cancer therapy," *IEEE J. Sel. Top. Quantum Electron.* **18**, 1367–1386 (2012).
8. L. C. Enfield, G. Cantanhede, D. Westbroek, M. Douek, A. D. Purushotham, J. C. Hebden, and A. P. Gibson, "Monitoring the response to primary medical therapy for breast cancer using three-dimensional time-resolved optical mammography." *Technol. Cancer Res. Treat.* **10**, 533–547 (2011).
9. H. Soliman, A. Gunasekara, M. Rycroft, J. Zubovits, R. Dent, J. Spayne, M. Yaffe, and G. Czarnota, "Functional imaging using diffuse optical spectroscopy of neoadjuvant chemotherapy response in women with locally advanced breast cancer," *Clin. Cancer Res.* **16**, 2605–2614 (2010).
10. B. J. Tromberg, B. W. Pogue, K. D. Paulsen, A. G. Yodh, D. A. Boas, and A. E. Cerussi, "Assessing the future of diffuse optical imaging technologies for breast cancer management," *Med. Phys.* **35**, 2443–2451 (2008).
11. D. R. Busch, W. Guo, R. Choe, T. Durduran, M. D. Feldman, C. Mies, M. A. Rosen, M. D. Schnall, B. J. Czerniecki, J. Tchou, A. DeMichele, M. E. Putt, and A. G. Yodh, "Computer aided automatic detection of malignant lesions in diffuse optical mammography," *Med. Phys.* **37**, 1840–1849 (2010).
12. R. Choe, S. D. Konecky, A. Corlu, K. Lee, T. Durduran, D. R. Busch, B. J. Czerniecki, J. Tchou, D. L. Fraker, A. DeMichele, B. Chance, S. R. Arridge, M. Schweiger, J. P. Culver, M. D. Schnall, M. E. Putt, M. A. Rosen, and A. G. Yodh, "Differentiation of benign and malignant breast tumors by in-vivo three-dimensional parallel-plate diffuse optical tomography," *J. Biomed. Opt.* **14**, 024020 (2009).
13. D. B. Jakubowski, A. E. Cerussi, F. Bevilacqua, N. Shah, D. Hsiang, J. Butler, and B. J. Tromberg, "Monitoring neoadjuvant chemotherapy in breast cancer using quantitative diffuse optical spectroscopy: a case study," *J. Biomed. Opt.* **9**, 230–238 (2004).
14. M. S. Pepe, *The Statistical Evaluation of Medical Tests for Classification and Prediction* (Oxford University Press, New York, 2003).
15. N. E. Breslow, N. E. Day, and W. Davis, *Statistical methods in cancer research (Vol. 1) The Analysis of Case control Studies*, No. 32 in IARC Scientific Publications (International Agency for Research on Cancer, 1980).
16. H. Dehghani, M. Eames, P. Yalavarthy, S. Davis, S. Srinivasan, C. Carpenter, B. W. Pogue, and K. D. Paulsen, "Near infrared optical tomography using NIRFAST: Algorithm for numerical model and image reconstruction," *Commun. Numer. Meth. Eng.* **25**, 711–732 (2009).
17. M. Jermyn, B. W. Pogue, H. Ghadyani, S. Davis, M. Mastanduno, and H. Dehghani, "A user-enabling visual workflow for near-infrared light transport modeling in tissue," in *Biomedical Optics*, OSA Technical Digest (Optical Society of America, 2012), paper BW1A.7.
18. A. Cerussi, D. Hsiang, N. Shah, R. Mehta, A. Durkin, J. Butler, and B. J. Tromberg, "Predicting response to breast cancer neoadjuvant chemotherapy using diffuse optical spectroscopy." *Proc. Natl. Acad. Sci.* **104**, 4014–4019 (2007).
19. Q. Zhu, S. Tannenbaum, P. Hegde, M. Kane, C. Xu, and S. H. Kurtzman, "Noninvasive monitoring of breast cancer during neoadjuvant chemotherapy using optical tomography with ultrasound localization." *Neoplasia* **10**, 1028–1040 (2008).
20. S. Jiang, B. W. Pogue, C. M. Carpenter, S. P. Poplack, W. A. Wells, C. A. Kogel, J. A. Forero, L. S. Muffly, G. N. Schwartz, K. D. Paulsen, and P. A. Kaufman, "Evaluation of breast tumor response to neoadjuvant chemotherapy with tomographic diffuse optical spectroscopy: case studies of tumor region-of-interest changes." *Radiology* **252**, 551–560 (2009).
21. M. G. Pakalniskis, W. A. Wells, M. C. Schwab, H. M. Froehlich, S. Jiang, Z. Li, T. D. Tosteson, S. P. Poplack, P. A. Kaufman, B. W. Pogue, and K. D. Paulsen, "Tumor angiogenesis change estimated by using diffuse optical spectroscopic tomography: demonstrated correlation in women undergoing neoadjuvant chemotherapy for invasive breast cancer?" *Radiology* **259**, 365–374 (2011).
22. A. E. Cerussi, V. W. Tanamai, D. Hsiang, J. Butler, R. S. Mehta, and B. J. Tromberg, "Diffuse optical spectroscopic imaging correlates with final pathological response in breast cancer neoadjuvant chemotherapy." *Philos. Trans. R. Soc. A* **369**, 4512–4530 (2011).
23. B. J. Tromberg, A. Cerussi, N. Shah, M. Compton, A. Durkin, D. Hsiang, J. Butler, and R. Mehta, "Imaging in breast cancer: diffuse optics in breast cancer: detecting tumors in pre-menopausal women and monitoring neoadjuvant chemotherapy." *Breast Cancer Res.* **7**, 279–285 (2005).
24. B. Chance, S. Nioka, J. Zhang, E. F. Conant, E. Hwang, S. Briest, S. G. Orel, M. D. Schnall, and B. J. Czerniecki, "Breast cancer detection based on incremental biochemical and physiological properties of breast cancers a six-year, two-site study," *Acad. Rad.* **12**, 925–933 (2005).

25. M. K. Simick, R. Jong, B. Wilson, and L. Lilge, "Non-ionizing near-infrared radiation transillumination spectroscopy for breast tissue density and assessment of breast cancer risk." *J. Biomed. Opt.* **9**, 794–803 (2004).
26. K. Blyschak, M. Simick, R. Jong, and L. Lilge, "Classification of breast tissue density by optical transillumination spectroscopy: optical and physiological effects governing predictive value," *Med. Phys.* **31**, 1398–1414 (2004).
27. X. Song, B. W. Pogue, S. Jiang, M. M. Dooley, H. Dehghani, T. D. Tosteson, and K. D. Paulsen, "Automated region detection based on the contrast-to-noise ratio in near-infrared tomography," *Appl. Opt.* **43**, 1053–1062 (2004).
28. S. Kukreti, A. Cerussi, B. Tromberg, and E. Gratton, "Intrinsic tumor biomarkers revealed by novel double-differential spectroscopic analysis of near-infrared spectra," *J. Biomed. Opt.* **12**, 020509–020509–3 (2007).

1. Introduction

An increasingly popular treatment protocol for breast cancer is neoadjuvant chemotherapy, which involves administration of chemotherapy drugs prior to surgical removal of the tumor tissue [1]. The treatment goal is to reduce the tumor size and eliminate or reduce micro-metastases before surgery. During treatment, it is desirable to observe the effects of particular drug regimens on tumor physiology which, in turn, could potentially permit early determination of the effectiveness of the chemotherapy regimen. For this reason, neoadjuvant chemotherapy monitoring is an active area of research in clinical medicine [2–4], including optical imaging and monitoring [5–10].

Diffuse Optical Tomography (DOT) is an evolving biomedical optics technique that readily provides full three-dimensional (3D) images of tissue hemoglobin concentration, blood oxygen saturation, and optical scattering coefficients in breast tissue. Recently, we developed a statistical image analysis technique for DOT [11] and applied it to a breast cancer data set [12]. The statistical approach derives a probability of malignancy signature for normal and cancerous tissues based on a collection of optical parameters within each subject and across the full subject population. Specifically, the approach converts 3D DOT reconstructions of total hemoglobin concentration, blood oxygen saturation, and tissue scattering coefficient into a single 3D DOT-based *probability of malignancy* image, which, in turn, enables volumetric segmentation of the tissue into 'normal' and 'cancerous' regions.

In this contribution we explore application of this statistical image analysis technique for monitoring the evolving tumor physiology of three subjects undergoing neoadjuvant chemotherapy. Our investigation acquires and employs DOT images of chemotherapy-patient breasts, along with probability of malignancy training set data. We show how to adapt these statistical imaging concepts to the chemotherapy monitoring problem; we measure longitudinal changes in tumor-region probability of malignancy during chemotherapy, and we compare these variations to those of clinical radiology. Finally, we find, in this limited data set, that the novel statistical image analysis scheme appears useful for prediction of chemotherapy response during the course of therapy, especially when compared to more traditional DOT quantification schemes. Thus, the results from this pilot study suggest that the probability of malignancy approach to DOT data holds potential to provide useful quantitative information about therapeutic effects during neoadjuvant chemotherapy.

2. Study populations

2.1. The training data set

Optical tomograms were collected on a population of 30 biopsy-confirmed lesions (i.e., the training set), and logistic regression was used to generate an optimized weighting vector for computation of tissue probability of malignancy based on optically measured total hemoglobin concentration, blood oxygen saturation, and reduced scattering coefficient [11]. Our training population consisted of 30 subjects with Invasive Ductal Carcinoma (IDC) and with or without

an associated Ductal Carcinoma *In Situ* (DCIS); the demographic details of this population are described in Table 1. Note, we have matched the diagnosis in the training set to that of the test set (available from pre-therapy biopsy, Section 2.2). We also compared results utilizing a training subset of only the post-menopausal subjects (N=14) and utilizing an expanded training set with a few more additional diagnoses (N=35). While small differences were found, our major conclusions were not changed by these choices of training set data. The results from the full training data set (N=35) (i.e., the training set employed in Ref. [11]) are given in the appendix (Section A.3).

Table 1. Demographic breakdown of cancers used to derive the probability of malignancy in this study.

Diagnosis	#	Age [yrs]	BMI [kg/m ²]	Tumor Size [cm ³]
IDC	8	44±11	27.4±6.2	2.9±1.2
IDC & DCIS	22	49±10	27.5±7.0	1.8±0.97
	30	48±10	27.5±6.7	2.1±1.1

IDC: Invasive Ductal Carcinoma; DCIS: Ductal Carcinoma *In Situ*; BMI: Body Mass Index. Numeric data is given as mean \pm standard deviation. 16 subjects were pre-menopausal and 14 were post-menopausal. The tumor size reported here is the longest dimension recorded in clinical radiology reports. These subjects are a subset of the population described in [12] with selection criteria described in [11].

2.2. The test data set

We applied the probability of malignancy weighting scheme to data from three new subjects who were imaged by DOT during neoadjuvant chemotherapy. The subjects received four cycles of Adriamycin with Cyclophosphamide and then three or four cycles of Taxane every two to three weeks. Two subjects (1 and 2) were post-menopausal at the beginning of therapy. Subject 3 was peri-menopausal when therapy began and was post-menopausal after therapy. The first DOT measurements were made prior to or within the first chemotherapy cycle, and subsequent measurements were made at various time points thereafter.

The subjects were imaged with standard clinical techniques (Subject 3, X-Ray mammogram and ultrasound) or were recruited into a research study with serial MR imaging (Subjects 1 and 2). Optical imaging was performed opportunistically throughout the course of patient treatment. Details for each subject are given in the appendix (Section A.1).

We determined the tumor region, or tumor volumetric mask, in two ways. The primary technique, presented in the main text, derived a tumor mask at each time point for the test subjects by (1) identifying the tumor location (e.g., from MRI), (2) identifying the nearby local maximum in the probability of malignancy distribution, $P(\mathcal{M})$, and then (3) creating the tumor mask by use of a region growing algorithm [12] based on $P(\mathcal{M})$. This algorithm gave tumor dimensions that were constrained by the maximum size of the tumor as extracted from radiology reports (i.e., pre-therapy size) and by the size corresponding to tissue boundaries at 25% of the local maximum in $P(\mathcal{M})$. A second approach, presented in the appendix (Section A.2), derived a single tumor mask from data at the first time point using the same region growing algorithm based on the tissue attenuation coefficient [12]; this mask was then held constant for all chemotherapy time points. This second approach essentially makes an assumption that the tumor is in roughly the same geometrical position for each serial image (see Section A.2). In both approaches, we determined the healthy tissue as any region of the breast excepting the tumor, excepting a 2 cm penumbra around the tumor, and excepting all tissues within 1 cm of

the breast compression plates. Note, as will be seen later in the paper (and appendix), use of one or the other of these two methods of segmentation did not significantly modify our major conclusions.

Several approaches could be used for normalization, and it is not *a priori* clear which approach is optimal. This is especially true since chemotherapy affects both normal and tumor tissue, i.e., it produces changes in optically measured physiological properties of both tissue types [13]. Here, for example, we have chosen to normalize the tissue optical properties in each subject to data taken from the patient's healthy tissue at the first time point. Then we follow the patient's probability of malignancy parameter over the treatment time course. The differences between subjects with complete versus incomplete responses to chemotherapy were thus characterized. For completeness, we also examined the effects of a second normalization approach, i.e., normalization to healthy tissue optical properties at each time point.

Finally, systematic errors were minimized, and tissue changes due to chemotherapy emphasized, by choosing a test data set such that only those subjects imaged in similar geometries throughout the course of their chemotherapy were selected (i.e., same compression plate separations, breast positioning, etc.).

3. Method

Broadly, the data processing procedure can be broken down into several distinct steps: (1) Identification of the cancer signature from the training set data (Section 3.1); (2) Normalization of time course data in a new (test) subject using logarithmic and Z-Score transformations (Section 3.2); (3) Calculation of probability of malignancy images for new (test) subjects at each accessible imaging time point during neoadjuvant chemotherapy (Section 3.3). A schematic of this process is provided in Fig. 1.

3.1. Training data set

A detailed explanation of the technique to derive a probability of malignancy for each voxel of the 3D tomogram of the cancer-bearing breast can be found in Ref. [11]. Note, we have matched the diagnosis in the training set to that of the test set (using information available from pre-therapy biopsy). Briefly, we identified 'normal' breast tissue in each subject and log-transformed each reconstructed parameter (total hemoglobin concentration, Hb_t ; blood oxygen saturation, StO_2 ; and reduced scattering coefficient, μ'_s) in each tissue voxel. The log-transformed data were then normalized using healthy-tissue averages to derive a 'Z-Score' for each parameter in each tissue voxel (e.g., the difference of tissue voxel property "Ln(X)" and its corresponding mean in the healthy-tissue region was determined, and the result was then divided by the standard deviation of "Ln(X)" in the healthy region). For example, the 'Z-Score' for total hemoglobin is

$$zHb_t = \frac{\ln[Hb_t] - \langle \ln[Hb_t] \rangle_H}{\sigma[\ln[Hb_t]]_H}. \quad (1)$$

Here, the subscript index H specifies the healthy tissue region. Notice, the denominator is the standard deviation (σ) of the log-transformed voxel data in the patient's healthy tissue. We note that inter-subject variations in healthy tissue (due to age, body mass index, menopausal status, etc.) are significantly reduced in these normalized data [11]. The statistical approach employs these Z-scores for total hemoglobin (zHb_t), scattering ($z\mu'_s$), and blood oxygen saturation ($zStO_2$).

The 'Malignancy Parameter' (\mathcal{M}) at each position (\vec{r}) within the breast is defined as

$$\mathcal{M}(\vec{r}) = [zHb_t(\vec{r}), zStO_2(\vec{r}), z\mu'_s(\vec{r}), 1] \cdot \vec{\beta} \quad (2)$$

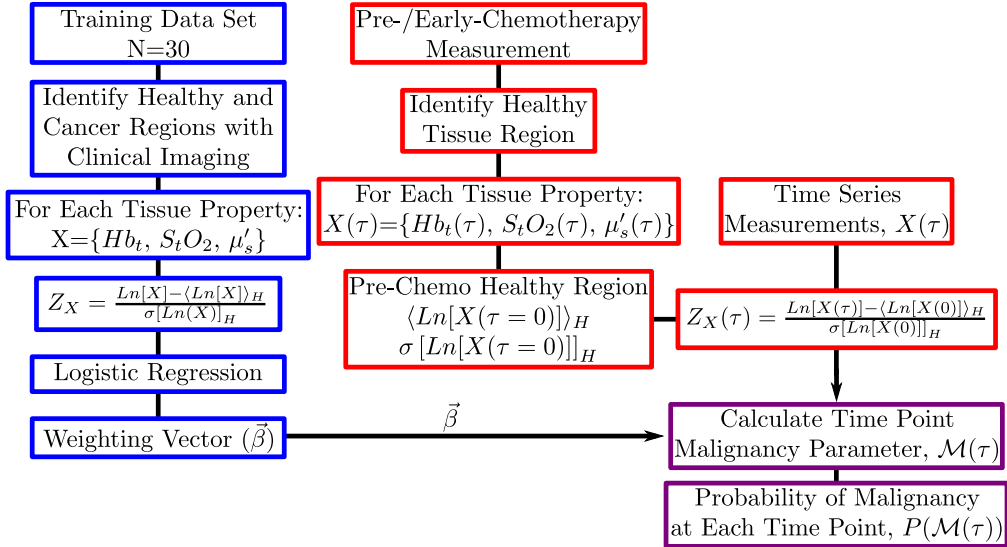


Fig. 1. Data processing flow chart for a single subject with multiple measurements while undergoing neoadjuvant chemotherapy. The weighting vector ($\vec{\beta}$, defining a ‘signature of malignancy’) is derived from a population of 30 biopsy confirmed cancers (blue boxes, Section 3.1). It essentially provides a weighting for each optical parameter per its importance for malignancy. Data is then normalized with logarithmic and Z-Score transformations for each subject across multiple time points designated by τ , red boxes, Section 3.2) using the mean ($\langle \ln[X(0)] \rangle_H$) and standard deviation ($\sigma[\ln[X(0)]]_H$) of healthy tissue from the earliest available time-point ($\tau = 0$) during the process. This normalized data is combined with $\vec{\beta}$ to produce a probability of malignancy for each patient and at each time point (purple boxes, Section 3.3).

where the last term in the data vector accounts for effects due to parameters not considered in the current analysis (see Refs. [14, 15]). Logistic regression is then applied to optimize the weighting vector ($\vec{\beta}$). That is, from \mathcal{M} , we compute a tissue (voxel) probability of malignancy using the probability of malignancy function, $P(\mathcal{M})$, i.e.,

$$P(\mathcal{M}(\vec{r})) = \frac{1}{1 + e^{-\mathcal{M}(\vec{r})}}, \quad (3)$$

and we optimize $\vec{\beta}$ such that the difference between healthy ($P(\mathcal{M}_H) \sim 0$) and malignant ($P(\mathcal{M}_M) \sim 1$) tissues in our training set is maximized. The resultant weighting vector ($\vec{\beta}$) was tested for generalizability using a leave-one-out protocol in a population of 35 biopsy confirmed lesions [11]. For the present study, to maximize connections between test and training sets we utilized the $\vec{\beta}$ derived from a subset of our total population (diagnosis of IDC or DCIS+IDC, $N=30$) ($\langle \beta_{zHb_t} \rangle = 0.93$, $\langle \beta_{zStO_2} \rangle = -0.42$, $\langle \beta_{zμ'_s} \rangle = 3.62$, $\langle β_0 \rangle = -5.67$).

3.2. Normalization for serial imaging (test set)

Chemotherapy affects both healthy and tumor tissue, changing the optically derived physiological properties [13]. We therefore choose to modify our previously described procedure [11] slightly by using parameters extracted from healthy tissue measured at a pre- or early-chemotherapy time point for the Z-scores (see Eqn. (4)). In one subject, we lacked a pre-chemotherapy time point; in this case we utilized healthy-tissue obtained at the first available

time point, taken between the first and second chemotherapy cycles, in order to derive the Z-scores. This choice of Z-score healthy-tissue-normalization emphasizes changes in physiological properties during the course of chemotherapy by comparing to *pre-/early-chemotherapy healthy-tissue* rather than comparing to the difference between tumor- and healthy-tissue at each time point. (For completeness, however, we also investigated the latter normalization scheme (see Section 4).)

As an example, we normalize total hemoglobin concentration (Hb_t) in a single tissue voxel according to the formula:

$$zHb_t(\tau) = \frac{\ln[Hb_t(\tau)] - \langle \ln[Hb_t(\tau = 0)] \rangle_H}{\sigma[\ln[Hb_t(\tau = 0)]]_H}. \quad (4)$$

Here, zHb_t is the Z-Score total hemoglobin concentration. Again, the subscript index H specifies the healthy tissue region. Time points are designated by τ ; $\tau = 0$ is the baseline measurement. Notice, the denominator is the standard deviation (σ) of the log-transformed hemoglobin data in the patient's pre-/early-chemotherapy healthy-tissue. (Note, parameters, i.e., $\vec{\beta}$, are derived from the various training sets using the approach in our previous work, Ref. [11].)

3.3. Application to serial chemotherapy imaging

We employed the optimized weighting vector, $\vec{\beta}$ (Section 3.1), to generate a 3D malignancy parameter map for each time point with Z-scores normalized by healthy-tissue at a pre-/early-chemotherapy time point (e.g., Eqn. (4)). We then calculated a 3D probability of malignancy tomogram from the malignancy parameter tomogram, i.e.,

$$\mathcal{M}(\vec{r}, \tau) = [zHb_t(\vec{r}, \tau), zStO_2(\vec{r}, \tau), z\mu'_s(\vec{r}, \tau), 1] \cdot \vec{\beta}, \quad (5)$$

$$P(\mathcal{M}) = P(\mathcal{M}(\vec{r}, \tau)) = \frac{1}{1 + e^{-\mathcal{M}(\vec{r}, \tau)}} \quad (6)$$

where \vec{r} is the spatial position of each voxel and other variables were previously defined. Using a 3D region growing algorithm [12] based on a tumor location defined by clinical imaging, we can readily identify the spatial extent of the tumor in DOT images. We performed this spatial segmentation at each time point (Section 2.2) based on $P(\mathcal{M})$. As noted earlier (Section 2.2), we also utilized the spatial mask derived from the first time point to segment the healthy and tumor tissue at all time points (see appendix, Section A.2). Both techniques led us to similar primary conclusions, but we use the per-time-point region approach in the main text, because this scheme accounts better for uncontrolled changes in geometry.

Several metrics can be used to extract comparative information from this data, and while quantitatively different, they lead to similar conclusions. A metric that captures both changes in tumor volume and magnitude of $P(\mathcal{M})$ essentially sums $P(\mathcal{M})$ over the tumor region or healthy region. We use these parameters, i.e.,

$$S_H(\tau) = \sum_{\text{Healthy Voxels}} P(\mathcal{M}(\vec{r}, \tau)) \quad (7)$$

$$S_M(\tau) = \sum_{\text{Malignant Voxels}} P(\mathcal{M}(\vec{r}, \tau)), \quad (8)$$

for tracking the responses to chemotherapy and comparing responders to partial-responders.

3.4. MRI segmentation

Two subjects (1 and 2) also took part in a Dynamic Contrast Enhanced MRI (DCE-MRI) imaging study, and these data were available to extract 3D tumor volumes. We utilized contrast

enhanced subtraction images taken approximately 10 minutes after injection of Gadolinium Diethylenetriamine Penta-acetic Acid (Gd-DTPA). Segmentation was accomplished by thresholding image data at 3.5 times the signal level of fatty tissue, then smoothing the edges [16, 17]. Artifacts (primarily at the skin-air boundary) were removed manually.

4. Results and discussion

The procedure described in the previous section produces a 3D map of the probability of malignancy at each time point during chemotherapy. Example slices through the center of the tumor in the malignancy maps of Subject 2 are shown in Fig. 2. Notice that the probability of malignancy in the tumor region decreases significantly over time; by the last time point (post-chemotherapy, pre-surgery), the probability of malignancy has only a few scattered non-zero regions. This prediction was later validated by histology which determined that Subject 2 had complete pathologic response to chemotherapy.

In Fig. 3 we show fractional changes in the summed malignancy parameter, $S_d(\tau)$ (where $d = H, M$), for the healthy and malignant tissues of each patient during neoadjuvant chemotherapy.

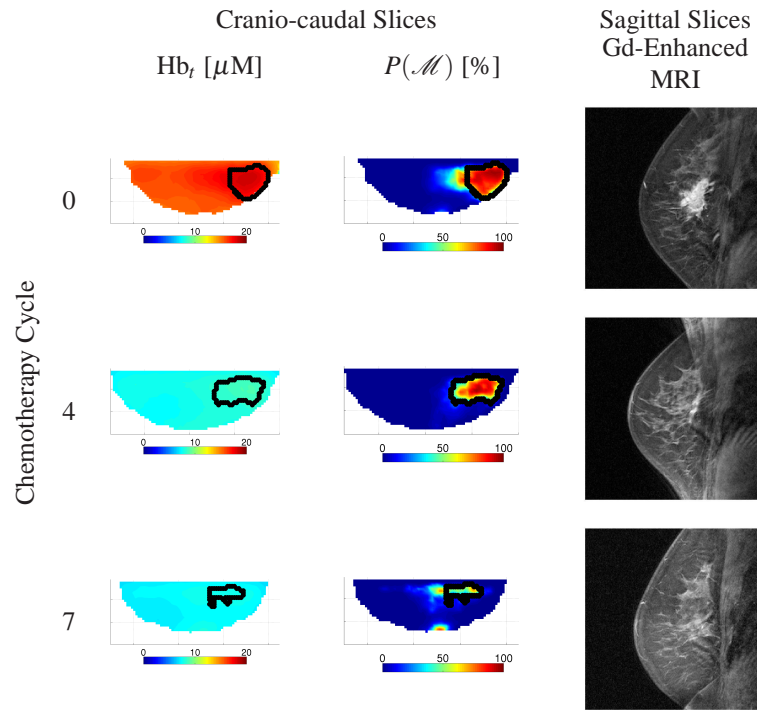


Fig. 2. Subject 2. Cranio-caudal slices through the center of a tumor located in the upper right of this image from a 3D reconstruction of Hb_t and the probability of malignancy, $P(\mathcal{M})$, at three time points during neoadjuvant chemotherapy. Data shown was collected prior to the start of chemotherapy (top), after 4 cycles of Adriamycin + Cyclophosphamide (middle), and after an additional 3 cycles of Taxane (bottom). Gd-enhanced MRI subtraction images were collected ~ 10 min. after injection. MRI images are scaled individually to improve visibility. Due to differences in equipment geometry, the optical and MR images were acquired in different planes. The tumor boundary is marked by black line contours in both the Hb_t and $P(\mathcal{M})$ images. $P(\mathcal{M})$ was calculated from a training set of IDC and IDC+DCIS subjects ($N=30$).

apy. (Note, unless stated otherwise in the caption, dashed (solid) lines correspond to malignant (healthy) tissues.) Results using two training sets are shown. One training set had all subjects with IDC or IDC+DCIS (N=30); the other training set used only post-menopausal subjects with IDC or IDC+DCIS (N=14). Subjects 1 and 2 were complete responders as determined by MRI and pathology, and Subject 3 was a partial responder by ultrasound and pathology. We see that Subject 3, with a partial pathological response, exhibited a rise in $S_M(\tau)$ over the course of her therapy, while in Subjects 1 and 2, $S_M(\tau)$ fell with time. These data have limitations. Unfortunately, Subject 3 left the study prior to acquisition of later time points, and Subject 1 did not join our study until after her first dose of chemotherapy. Thus, even though Z-score variables are employed instead of absolute properties, these results should be interpreted with caution. With these caveats, the observations clearly reveal the potential utility of the probability of malignancy scheme for monitoring chemotherapy.

We also performed the analysis described in Section 3.3 with a modification of the normalization procedure (previously described in Section 3.2), in this case utilizing the healthy tissue at each chemotherapy time point for normalization (i.e., $\langle \ln[Hb_t(0)] \rangle_H \rightarrow \langle \ln[Hb_t(\tau)] \rangle_H$; $\sigma[\ln[Hb_t(0)]]_H \rightarrow \sigma[\ln[Hb_t(\tau)]]_H$ in Eqn. (4)). The resulting changes in our calculated probability of malignancy during the course of chemotherapy are shown in Fig. 4. We were unable to discriminate between the partial and complete chemotherapeutic responses using the new normalization scheme in the same limited sample. These effects are possibly due to concurrent changes in healthy tissue as a result of the chemotherapy. Thus it appears desirable to normalize using healthy tissue at an “early” time point, rather than serially at each time point in the chemotherapy process.

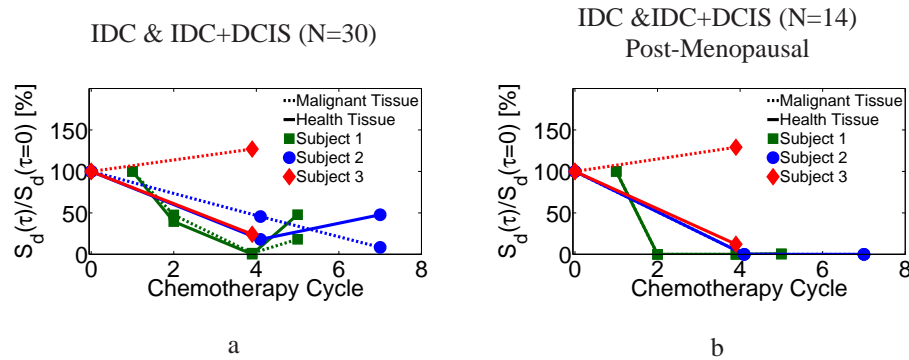


Fig. 3. Fractional change in S_d for healthy ($d = H$) and malignant ($d = M$) tissues. In calculating $P(\mathcal{M})$, data are normalized to healthy tissue at the *first* optical measurement using a training set of subjects with IDC or IDC+DCIS (a, N=30) or post-menopausal subjects with IDC or IDC+DCIS (b, N=14). Tumor tissue ($S_M(\tau)$) is denoted with dashed lines and healthy tissue ($S_H(\tau)$) with solid lines. Subjects 1 and 2 were complete responders by pathology. Subject 3 was a partial responder by pathology. Note, Subject 1 did not have an optical measurement prior to beginning chemotherapy, and the $\tau = 0$ time point is defined to be 100%. In panel b, Subjects 1 and 2 have very low $S_M(\tau)$ and $S_H(\tau)$ in both the tumor and healthy tissue at later time points, resulting in overlapping traces.

We utilized DCE-MRI to measure tumor volume at each time point for Subjects 1 and 2 and then compared DCE-MRI data to our calculated $S_M(\tau)$. In Fig. 5, the changes in these MRI volumes are directly compared to $S_M(\tau)$. Both metrics showed similar changes over the course of therapy. This segmentation does not take into account the overall impression of the clinical

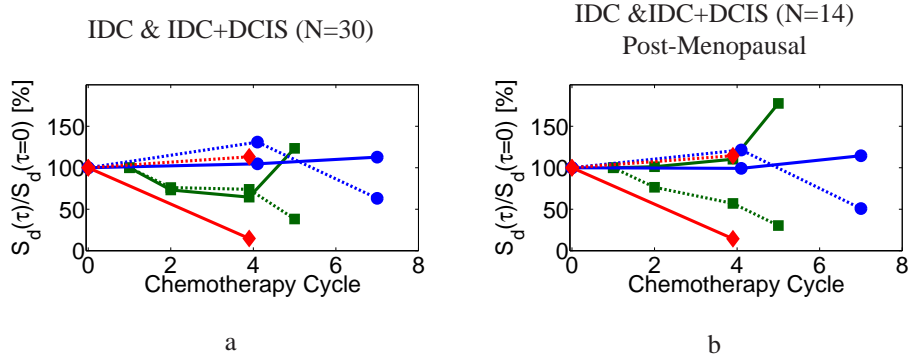


Fig. 4. Fractional change in S_d for healthy ($d = H$) and malignant ($d = M$) tissues. In calculating $P(\mathcal{M})$, data are normalized to healthy tissue at the *each* optical measurement time point using a training set of subjects with IDC or IDC+DCIS (a, $N=30$) or post-menopausal subjects with IDC or IDC+DCIS (b, $N=14$). Tumor tissue ($S_M(\tau)$) is denoted with dashed lines and healthy tissue ($S_H(\tau)$) with solid lines. The legend is the same as Fig. 3; only the normalization scheme is changed.

radiologist, leading to some discrepancy between the calculated volume and radiological impression, e.g., Subject 2 has a complete response by pathology and radiology, but had a 1.6 cc segmented cancer volume at the end of treatment. (Note, Subject 3 was not imaged with MRI, and we are therefore unable to report changes in her tumor volume.)

Subject 3 exhibited a partial response (~ 1.6 and 0.2 cm residual cancer foci at surgery) to chemotherapy in both imaging (mammography and ultrasound) and pathology. Previous work has suggested that partial responders to chemotherapy may have significantly different optical signatures (e.g., Ref. [6,9,18–22]). Encouragingly, the results of the present pilot study based on tumor probability of malignancy trajectories are in line with these earlier contributions. Note, however, the results of the present study are suggestive but preliminary, because the population is small and the number of time points few.

One of the advantages of multi-wavelength diffuse optical techniques is the simultaneous measurement of multiple physiologically relevant chromophores, providing the opportunity for multi-dimensional data analysis. We also extracted time courses of the response to chemotherapy for Hb_t , StO_2 , and μ'_s , but no obvious trend separating responding and partial-responding subjects was apparent in these data (Fig. 6). Several research groups have previously examined metrics for cancer detection or chemotherapy tracking combining multiple chromophores with hypothesis-driven [12, 23] or data-set derived [24–28] functions. Our study further illustrates the potential of optical metrics derived from multiple physiological parameters as a means to assess the efficacy of chemotherapy.

Finally, the present work tracking tumor variation due to neoadjuvant chemotherapy is notable, in part because it applies a signature derived from DOT measurements of a population of known cancers in a completely different study. Thus the pilot study suggests that such signatures may be robust, and points to the promise of using such signatures for tracking and modifying the course of chemotherapy treatment with relatively inexpensive and non-ionizing diffuse optical systems. It lays more groundwork towards use of Computer Aided Detection schemes based on DOT (i.e., DOT-CAD).

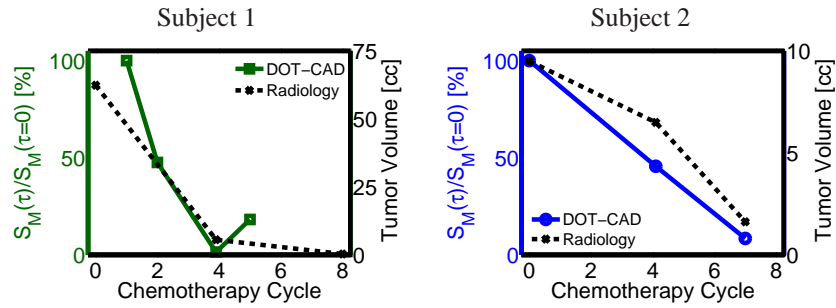


Fig. 5. Fractional change in predicted response to chemotherapy using tumor $S_M(\tau)$ (normalized to initial time point) and change in tumor volume measured by MRI relative to initial measurements. Results from DOT-CAD ($S_M(\tau)$, solid lines) were calculated from a training set of IDC and IDC+DCIS subjects ($N=30$), normalized to the pre-/early-chemotherapy time point. Note: MRI volumes were obtained by a simple segmentation of late contrast enhanced subtraction images and *do not* include the overall radiological impression (dashed lines). Subject 3 was not imaged with MRI during the course of her treatment.

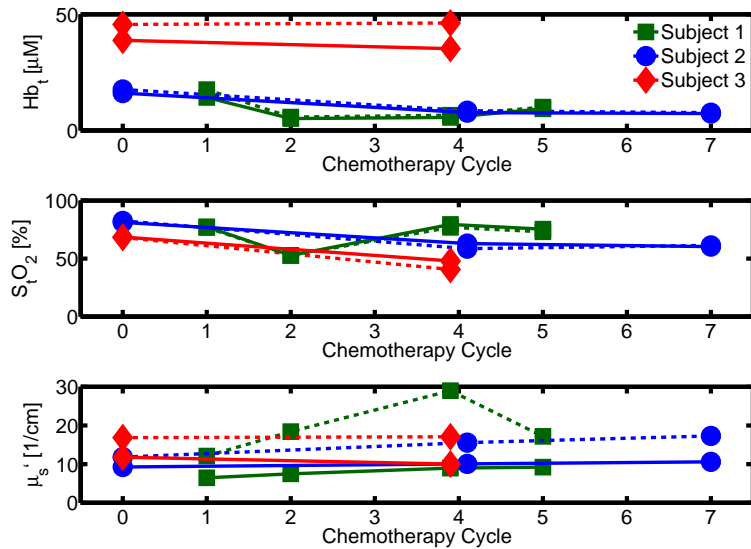


Fig. 6. Hb_t , StO_2 , and μ'_s as a function of chemotherapy cycle for Subjects 1-3. Dashed (solid) lines denote the average value in malignant (healthy) tissue. The obvious trends found in this paper, utilizing the probability of malignancy approach, are not apparent in this un-normalized and un-weighted data. Masks were derived from region growing on $P(\mathcal{M})$ (Section 3.3, i.e., as in Fig. 2).

5. Conclusion

We have introduced and demonstrated a statistical technique for automated analysis of tumor response to neoadjuvant chemotherapy. The method utilizes the *probability of malignancy* concept; coefficients of a malignancy parameter derived from a population of known cancers were applied in patients undergoing neoadjuvant chemotherapy to assess therapeutic response. The probability of malignancy in the tumor region differed significantly during the course of treatment in two complete responders compared to the partial responder. Interestingly, clear distinctions between the responding and partially-responding patients were not evident in single parameter (Hb_t , StO_2 , μ_s') analyses. Thus the multiparameter analysis of DOT data appears to provide additional diagnostic merit that is not apparent in the univariate analysis of individual optical properties.

In total, the pilot study suggests that variation of a composite cancer signature measured by diffuse optical tomography, i.e., the malignancy parameter, may be an effective means for monitoring the progression and efficacy of neoadjuvant chemotherapy. Further study of this approach is warranted. Clearly, the present work represents a proof of principle and will require more subjects for full validation of this preliminary result.

A. Appendix

In this section, we provide detailed demographic data and clinical time lines for each subject (Section A.1), and we also provide results for therapeutic responses that utilized constant tissue segmentation derived from the initial measurement (Section A.2) and a somewhat larger training set (Section A.3).

A.1. Detailed test subjects information

Detailed information on each subject in the test data set is found in Table 2, Table 3, and Table 4. Each subject underwent a slightly different time course of chemotherapy doses. We therefore made the decision to scale each time course according to the patient's chemotherapy cycle, i.e., the number of chemotherapy doses she had received up to that point.

Table 2. Subject 1.

Cycle	Week	Subject 1, Age 51 yr., BMI 34.9 kg/m ²
		Notes
	-1	Biopsy: IDC/DCIS
0	0	Baseline MRI
1.0	1.0	Chemotherapy Begins
1.0	3.0	DOT Baseline
2.0	6.0	DOT
3.9	11.6	DOT
3.9	11.6	MRI marked decrease in enhancement
5.0	15.0	DOT
7.9	23.9	MRI
post	26.7	Surgical Pathology: complete response

Timeline is zeroed at the beginning of chemotherapy. No metastatic carcinoma cells were found in axillary lymph nodes after surgery. IDC: Invasive Ductal Carcinoma; DCIS: Ductal Carcinoma *In Situ*. 8 total cycles of chemotherapy.

Table 3. Subject 2.

Subject 2, Age 51 yr., BMI 24.3 kg/m ²		
Cycle	Week	Notes
0	0	Biopsy: IDC
0	0	Baseline MRI
0	0	DOT Baseline
1.0	1.0	Chemotherapy Begins
1.0	1.0	Biopsy: IDC, no change
4.1	8.1	MRI: much less enhancement
4.1	8.1	DOT
7.0	16.7	MRI: complete response
7.0	16.7	DOT
post	20	Surgical Pathology: complete response

Timeline is zeroed at the beginning of chemotherapy. No metastatic carcinoma cells were found in axillary lymph nodes after surgery. IDC: Invasive Ductal Carcinoma. 7 total cycles of chemotherapy.

Table 4. Subject 3.

Subject 3, Age 47 yr., BMI 22.1 kg/m ²		
Cycle	Week	Notes
0	-3	Biopsy: IDC/DCIS
0	0	DOT Baseline
1.0	1.0	Chemotherapy Begins
3.9	5.9	DOT
post	17.7	Surgical Pathology: 2 foci of IDC (1.6 and 0.2 cm)

This subject did not have MRI exams during her course of treatment. Timeline is zeroed at the beginning of chemotherapy. No metastatic carcinoma cells were found in axillary lymph nodes after surgery. IDC: Invasive Ductal Carcinoma; DCIS: Ductal Carcinoma *In Situ*. 7 total cycles of chemotherapy.

A.2. Constant tissue segmentation based on mask at initial time point

An example of data segmentation utilizing a fixed tumor boundary mask from the first time point is shown in Fig. 9. The discrepancies between $P(\mathcal{M})$ and the tissue segmentation are more significant than in the per-time point segmentation shown in Fig. 2. $S_d(\tau)$ for each region ($d = H$ and $d = M$) is shown in Fig. 7 (normalized to healthy tissue at the first optical data point) and Fig. 8 (normalized to healthy tissue at each time point). The subjects who responded completely to chemotherapy (1 and 2) can still be distinguished from the partially responding Subject 3.

A.3. Expanded training set to include additional diagnoses

In this section, we present results utilizing the entire (N=35) training set described in our previous work [11] (Table 5). This training set includes several subjects with invasive lobular carcinoma (ILC), a cancer which is not present in the test data set. Fig. 10 and Fig. 11 show the calculated probability of malignancy versus chemotherapy cycle using this expanded training set. The main results of the full analysis using all (N=35) training set subjects differ little from those presented in Fig. 3, as might be expected given the small number of additional training set subjects. Again, the normalization to healthy tissue at each time point does not appear to be effective in separating partial and complete responders (Fig. 11).

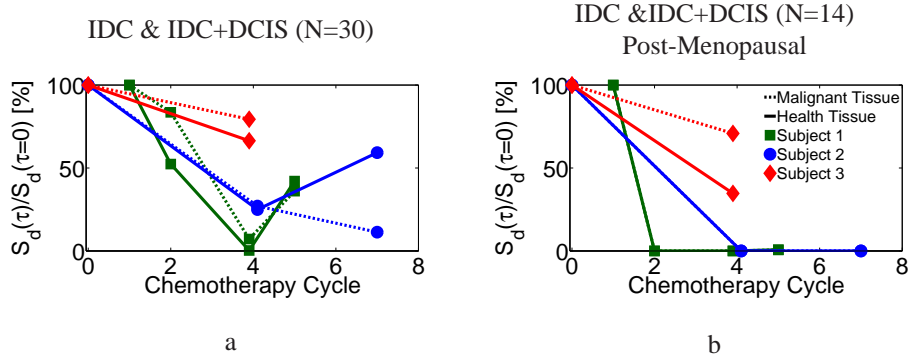


Fig. 7. Fractional change in $S_d(\tau)$ for healthy ($d = H$) and malignant ($d = M$) tissues versus chemotherapy cycle in three subjects, normalized to healthy tissue at the *first* optical measurement training set of subjects with IDC or IDC+DCIS (a, $N=30$) or post-menopausal subjects with IDC or IDC+DCIS (b, $N=14$). Tumor tissue ($S_M(\tau)$) is denoted with dashed lines and healthy tissue ($S_H(\tau)$) with solid lines. Subjects 1 and 2 were complete responders by pathology. Subject 3 was a partial responder by pathology. Note that Subject 1 did not have an optical measurement prior to beginning chemotherapy. The $S_M(\tau)$ and $S_H(\tau)$ in Subjects 1 and 2 are overlapping.

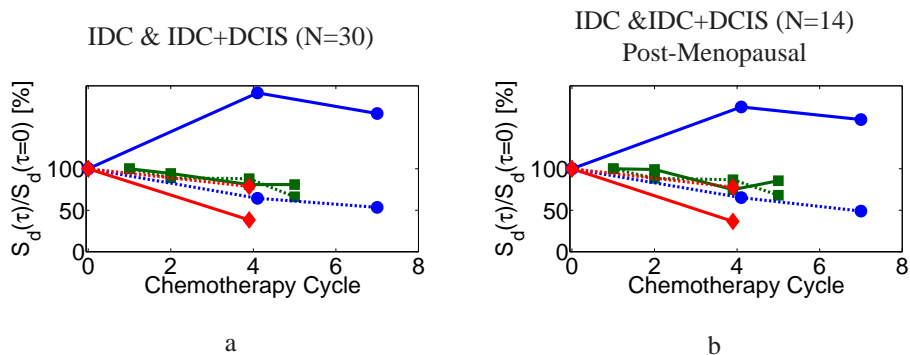


Fig. 8. Fractional change in $S_d(\tau)$ for healthy ($d = H$) and malignant ($d = M$) tissues versus chemotherapy cycle in three subjects, normalized to healthy tissue at *each* optical measurement training set of subjects with IDC or IDC+DCIS (a, $N=30$) or post-menopausal subjects with IDC or IDC+DCIS (b, $N=14$). Tumor tissue ($S_M(\tau)$) is denoted with dashed lines and healthy tissue ($S_H(\tau)$) with solid lines. The legend is the same as Fig. 7.

Table 5. Demographic breakdown of cancers used to derive the probability of malignancy presented in Section A.3.

Diagnosis	#	Age [yrs]	BMI [kg/m ²]	Tumor Size [cm ³]
IDC	8	44±11	27±6.2	2.9±1.2
IDC & DCIS	22	49±10	28±7	1.8±0.97
DCIS	2	60±4.9	29±6.6	0.7±0.28
ILC	2	62±3.5	22±2	1.4±0.35
DCIS & LCIS	1	39	19	5
	35	49±11	27±6.5	2.1±1.2

IDC: Invasive Ductal Carcinoma; DCIS: Ductal Carcinoma *In Situ*; ILC: Invasive Lobular Carcinoma; LCIS: Lobular Carcinoma *In Situ*; BMI: Body Mass Index. Numeric data is given as mean ± standard deviation. 16 subjects were pre-menopausal and 19 were post-menopausal. The tumor size reported here is the longest dimension recorded in clinical radiology reports. These subjects are a subset of the population described in [12] with selection criteria described in [11].

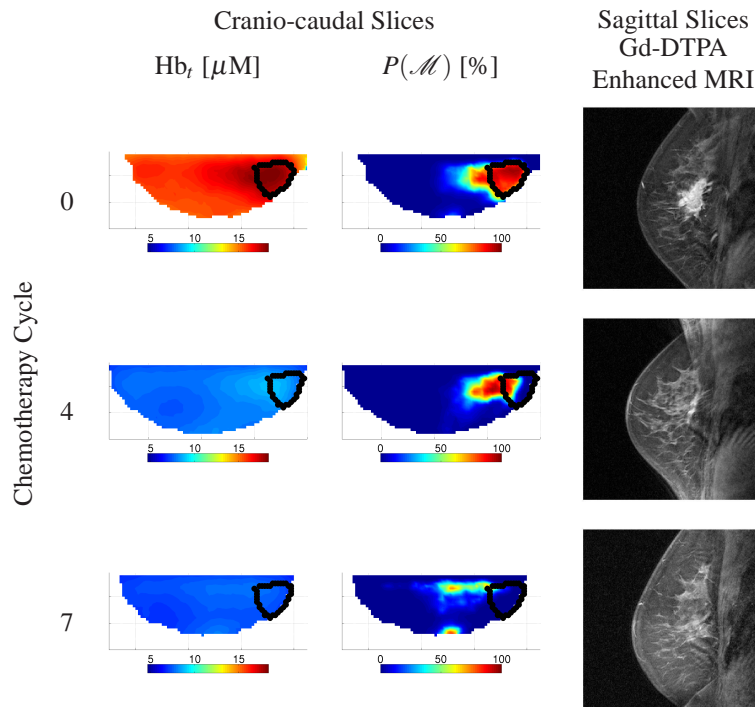


Fig. 9. Subject 2. Cranio-caudal slices through the center of a tumor located in the upper right of this image from a 3D reconstruction of Hb_t and the probability of malignancy, $P(\mathcal{M})$, at three time points during neoadjuvant chemotherapy. Data shown was collected prior to the start of chemotherapy (top), after 4 cycles of Adriamycin + Cyclophosphamide (middle), and after an additional 3 cycles of Taxane (bottom). MRI images are scaled individually to improve visibility. Note that the overall MRI contrast in chemotherapy cycle 4 is greatly reduced compared to baseline. Due to differences in equipment geometry, the optical and MR images were acquired in different planes. The tumor boundary is marked by black line contours in both the Hb_t and $P(\mathcal{M})$ images. $P(\mathcal{M})$ was calculated from a training set of IDC and IDC+DCIS subjects (N=30).

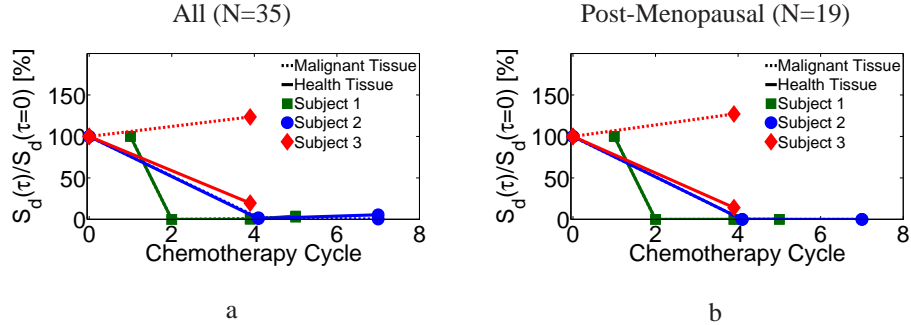


Fig. 10. Fractional change in S_d for healthy ($d = H$) and malignant ($d = M$) tissues. In calculating $P(\mathcal{M})$, data are normalized to healthy tissue measured at the *first* optical measurement using a mixed diagnoses training set (a, $N=35$, Table 5) or post-menopausal subjects with mixed diagnoses (b, $N=19$). Tumor tissue ($S_M(\tau)$) is denoted with dashed lines and healthy tissue ($S_H(\tau)$) with solid lines. Subjects 1 and 2 were complete responders by pathology. Subject 3 was a partial responder by pathology. Note that $S_M(\tau)$ and $S_H(\tau)$ in both Subjects 1 and 2 were barely distinguishable, i.e., the dashed and solid lines overlap.

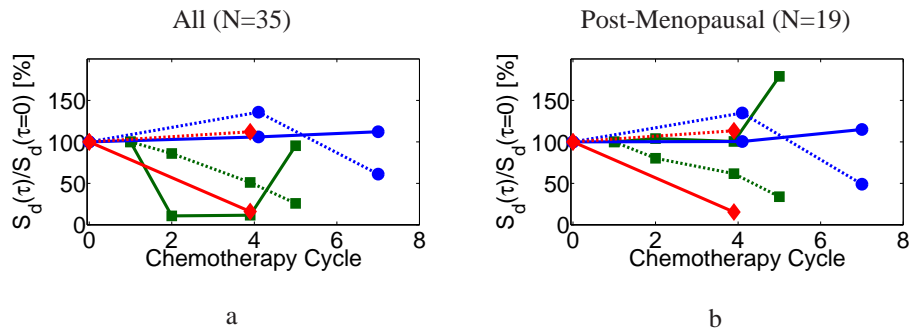


Fig. 11. Fractional change in S_d for healthy ($d = H$) and malignant ($d = M$) tissues. In calculating $P(\mathcal{M})$, data are normalized to healthy tissue measured at *each* each time point using a training set with mixed diagnoses (a, $N=35$, Table 5) or post-menopausal subjects with mixed diagnoses (b, $N=19$). Tumor tissue ($S_M(\tau)$) is denoted with dashed lines and healthy tissue ($S_H(\tau)$) with solid lines. The legend is the same as Fig. 10.

Acknowledgments

This work was supported by NIH grants R01-EB002109, K99-CA126187, P41-RR002305, and NTROI 1U54CA105480. The authors thank Norman Butler, and patient coordinators Kathleen Thomas, Tamara April, Deborah Arnold, Stephanie Damia, Dalton Hance, Monika Grosicka-Koptyra, Tiffany Averna, and Madeline E. Winters. We also thank colleagues who have contributed to this DOT breast program at Penn, including Britton Chance, John Schotland, Leonid Zubkov, Simon R. Arridge, Martin Schweiger, Joseph P. Culver, Soren D. Konecky, Alper Corlu, Kijoon Lee, Han Y. Ban, Saurav Pathak, and Douglas L. Fraker.